RSC Advances

PAPER

View Article Online
View Journal | View Issue

Check for updates

Cite this: *RSC Adv.*, 2024, **14**, 24574

A phytic acid-based CoMn bimetallic metal–organic aerogel (PA–CoMn-1 : x : 2 − x) as a modifier for electrochemical detection of non-steroidal anti-inflammatory drug 4-acetaminophenol†

Huijun Guo, * Yifei Qi, Guoxin Wang, Yue Zhang, Siqi Li and Boyu Tan

Received 31st May 2024
Accepted 18th July 2024

DOI: 10.1039/d4ra04012k

rsc.li/rsc-advances

Metal phosphides and phosphate-based materials have received significant attention due to their high electrocatalytic activity, adjustable structure composition and stability. Herein, we introduce a phytic acid-based CoMn bimetallic metal–organic (PA–CoMn) aerogel as an electrode modifier, derived from PA and mixed transition metal ions (Co^{2+}, Mn^{2+}). We explored its performance in the sensitive sensing of non-steroidal anti-inflammatory drug 4-acetaminophenol (4-AP) for the first time. We investigated the electrochemical behavior of the modified screen-printed carbon electrode (SPCE) by cyclic voltammetry (CV) and differential pulse voltammetry (DPV). The PA–CoMn-1 : 1.5 : 0.5 aerogel/Nafion/SPCE proved to be highly sensitive and selective towards the detection of 4-AP. A double linear response was recorded for 4-AP over the range of 1 μM to 0.1 mM and lower detection limits (LOD) of 0.2133 μM. The applicability of the PA–CoMn-1 : 1.5 : 0.5 aerogel/Nafion/SPCE in the detection of 4-AP in commercial drug samples with good recoveries was investigated, confirming the great potential of PA–CoMn-1 : 1.5 : 0.5 aerogel/SPCE in clinical applications.

1 Introduction

Drug safety in the environment has always been a widespread concern for humanity and is crucial to living organisms and ecosystem stability.[1] Drugs that stay unregulated or remain in the regularization cycle can cause an increase in the concentration of synthetic toxins in water bodies, creating a hidden risk of drinking water contamination.[2] Additionally, the physio-compound properties of acidic drugs may bring them through water treatment and filtration process, consequently creating a threat to drinking water supplies. In recent years, a large number of new trace pollutants, including pharmaceutical and personal care products (PPCPs), have been discovered in surface and groundwater sources of drinking water. PPCPs have high biological activity, which makes them difficult to completely remove through natural and biological degradation; hence, they have strong persistence in the environment.[3] The non-steroidal anti-inflammatory drug, 4-AP, has the characteristics of low toxicity, good curative effect, and few side effects. It is a typical PPCP pollutant and has been detected in many rivers in my country. It not only harms the balance of the aquatic ecosystem but also poses a threat to human health.[4] Currently, many methods, such as spectrophotometry,[5] high-performance liquid chromatography,[6] chemiluminescence,[7] fluorescence spectroscopy,[8] and capillary electrophoresis,[9] have been employed for the detection of 4-AP. However, the above methods have many shortcomings, including the need for complex preprocessing, being time-consuming, expensive, and requiring professionals. Therefore, the development of a facile and rapid analytical method with high selectivity and sensitivity for the sensing of 4-AP is particularly crucial in diagnostic applications and pharmaceutical fields. However, there are reports that portability, storage stability, and real-time sensing in electrochemical detection of 4-AP still need to be improved using an electrocatalyst.

The design of nanomaterials-based electrocatalysts with outstanding activity and a facile design of the electrochemical sensor is vital to accurately determine and quantify 4-AP. Metal phosphides and phosphate-based materials have recently been considered to be competitive candidates for electrocatalysis due to their high electrocatalytic activity, adjustable structural composition and stability.[10,11] Phosphates have been prepared through hydrothermal,[12] co-precipitation,[13,14] solvothermal,[15] atomic layer deposition,[16] and electrodeposition[17] methods. Organophosphorus-containing ligands have been used as precursors, including *O*-phospho-DL-serine[18] and PA. PA is a natural organic phosphorus resource containing six phosphoric acid groups, which can be obtained from plant seeds and

---

Center of Characterization and Analysis, Jinlin Institute of Chemical Technology, Jilin 132000, China. E-mail: m15981210065@163.com

† Electronic supplementary information (ESI) available. See DOI: https://doi.org/10.1039/d4ra04012k

grains and has a strong chelating ability. Currently, PA-based polymer gels have been developed[19] and PA-based materials are usually employed as precursors for further pyrolysis for electrocatalysis.[20–22] García-Dalí *et al.* exploited PA as a biosourced molecule and successfully prepared P-doped carbon-based hydrogen evolution reaction electrocatalysts with enhanced catalytic activity.[23] Huo *et al.* used PA as a doping biosourced molecule with two-dimensional PA doped co-metal–organic frameworks nanosheets for sensitive application in non-contact and multifunctional humidity sensors.[24] Feng *et al.* prepared bimetallic gel materials derived from PA and mixed Fe^{3+}/Co^{2+} transition metal ions and explored their performance in electrocatalytic oxygen evolution reaction, which has significant catalytic activity.[25] Incorporation of P into the carbon structure can have substantial effects on the chemical and physical properties of carbon materials. The presence of P modifies the electronic structure of carbons, thereby impacting the chemical reactivity of the material and altering the electrocatalytic properties.[26] Furthermore, the inclusion of P atoms in carbon materials has also been demonstrated to enhance chemical and electrochemical stability, rendering them more robust against degradation and deactivation.[27] Consequently, P has been considered "the next heteroatom to be explored" by the scientific community. Wang *et al.* exploited metal–organic aerogels (MOAs) with porous properties for colorimetric sensing of glucose.[28] Niu *et al.* prepared metal–organic framework $Ni_2(BDC)_2(DABCO)$ (Ni-MOF)/porous graphene aerogel (PGA) for application in simultaneous electrochemical determination of nitrochlorobenzene isomers with partial least squares.[29] Nevertheless, to our knowledge, few reports explore the preparation of PA–CoMn organic gel for drug sensing.

In this work, we prepared the PA–CoMn-1 : x : 2 − x (x = 0, 0.5, 1 and 1.5) gel from PA and mixed Co^{2+}/Mn^{2+} transition metal ions by facile and green one-pot synthesis under mild conditions. The resulting compounds exhibited promising properties, including high proton conductivity and self-foaming. To promote stability of the PA–CoMn-1 : x : 2 − x (x = 0, 0.5, 1 and 1.5) aerogel, we used the high-temperature carbonization method. We exploited PA–CoMn-1 : x : 2 − x (x = 0, 0.5, 1 and 1.5) aerogel as a matrix and dropped it on the surface of SPCE for the sensitive detection of 4-AP. The conductive and electrocatalytic properties of PA–CoMn-1 : x : 2 − x (x = 0, 0.5, 1 and 1.5) aerogel were analyzed using the CV and EIS technique. The experimental parameters for PA–CoMn-1 : x : 2 − x (x = 0, 0.5, 1 and 1.5) aerogel detection were optimized using the CV technique. With the optimized parameters, the DPV technique was used to achieve the low detection limit of 4-AP and it was applied to monitoring the 4-AP level in real samples of the commercialized tablet.

2 Experimental

2.1. Materials

Phytic acid solution (70% w/w H_2O), Nafion® (5% w/w in H_2O), $Co(NO_3)_2 \cdot 6H_2O$, $(CH_3COO)_2Mn$, *N*,*N*-dimethylformamide (DMF), and 4-acetaminophenol (4-AP) were purchased from Sigma-Aldrich. All chemicals were analytical grade and used without further purification. Phosphate buffer solution (PBS; 5 mM) was prepared by mixing the standard stock solutions of mono and disodium phosphate (NaH_2PO_4 and Na_2HPO_4). Diluted hydrochloric acid (HCl aq.) and sodium hydroxide (NaOH) were used for the preparation of solutions with different pH values. A real sample of the commercial drug was procured from local drug stores. All the solutions were prepared using doubly distilled (DD) water.

2.2. Instrumentation

To examine the formation and the phase of the material, X-ray diffraction (XRD) studies were carried out using the Empyrean (Cu Kα = 1.54 nm) instrument. Nicolet 6700 (Thermo Scientific) used to analyze FTIR analysis. Transmission electron microscopy (TEM) and energy-dispersive X-ray spectroscopy (EDS) of the sample were obtained using JEOL F200. The morphology was analyzed using a scanning electron microscope (SEM) (JSM-7610F Plus). The oxidation state and chemical composition of the material was identified using an ESCALAB 250 X-ray photoelectron spectroscopy (XPS) analyzer. The charge transfer resistance of the sensor was recorded using electrochemical impedance spectroscopy (EIS). The electrochemical characteristics of the electrodes were scrutinized by cyclic voltammetry (CV) and differential pulse voltammetry (DPV) instruments. All electrochemical tests were performed using Metrohm PGSTAT302N.

2.3. Preparation of PA–CoMn-1 : x : 2 − x (x = 0, 0.5, 1 and 1.5) organic gels

Preparation of PA–CoMn-1 : x : 2 − x (x = 0, 0.5, 1 and 1.5). When x = 1.5, the organic gel had the molecular formula PA–CoMn-1 : 1.5 : 0.5. The main preparation steps were as follows: a solution of PA (660.0 mg, 1 mmol) in DMF (1.0 mL) and a solution of $Co(NO_3)_2 \cdot 6H_2O$ (436.5 mg, 1.5 mmol) and $(CH_3COO)_2Mn$ (86.5 mg, 0.5 mmol) in DMF (1.0 mL) were fully mixed, and then heated at 80 °C for about 2.5 h. The solution mixture became turbid over time and a brown gel was obtained. The wet gel was soaked in DMF for one day to remove unreacted reactants, then subjected to solvent exchange in deionized water, and finally freeze-dried for 24 h to obtain the powder of aerogel PA–CoMn-1 : 1.5 : 0.5 gel.

Following a similar procedure, PA–Co-1 : 2 gel was prepared from PA (660.0 mg, 1 mmol) and $Co(NO_3)_2 \cdot 6H_2O$ (582.0 mg, 2.0 mmol). PA–Mn-1 : 2 gel was prepared from PA (660.0 mg, 1 mmol) and $(CH_3COO)_2Mn$ (346.0 mg, 2.0 mmol). PA–CoMn-1 : 1 : 1 gel was prepared from $Co(NO_3)_2 \cdot 6H_2O$ (291.0 mg, 1.0 mmol) and $(CH_3COO)_2Mn$ (173.0 mg, 1.0 mmol). PA–CoMn-1 : 0.5 : 1.5 gel was prepared from $Co(NO_3)_2 \cdot 6H_2O$ (145.5 mg, 0.5 mmol) and $(CH_3COO)_2Mn$ (259.5 mg, 1.5 mmol).

2.4. PA–CoMn-1 : x : 2 − x (x = 0,0.5, 1 and 1.5) gel carbonized at 800 °C

The resulting PA–CoMn-1 : x : 2 − x (x = 0, 0.5, 1 and 1.5) gel was heated under N_2 atmosphere at a heating rate of 5 °C min^{-1} to 800 °C, and kept at 800 °C for 2 h. After natural cooling, black powders of PA–CoMn-1 : x : 2 − x (x = 0.5, 1 and 1.5) aerogel were obtained. The entire synthesis method of the electrode modifier and the detection mechanism of 4-AP are shown in Scheme 1.

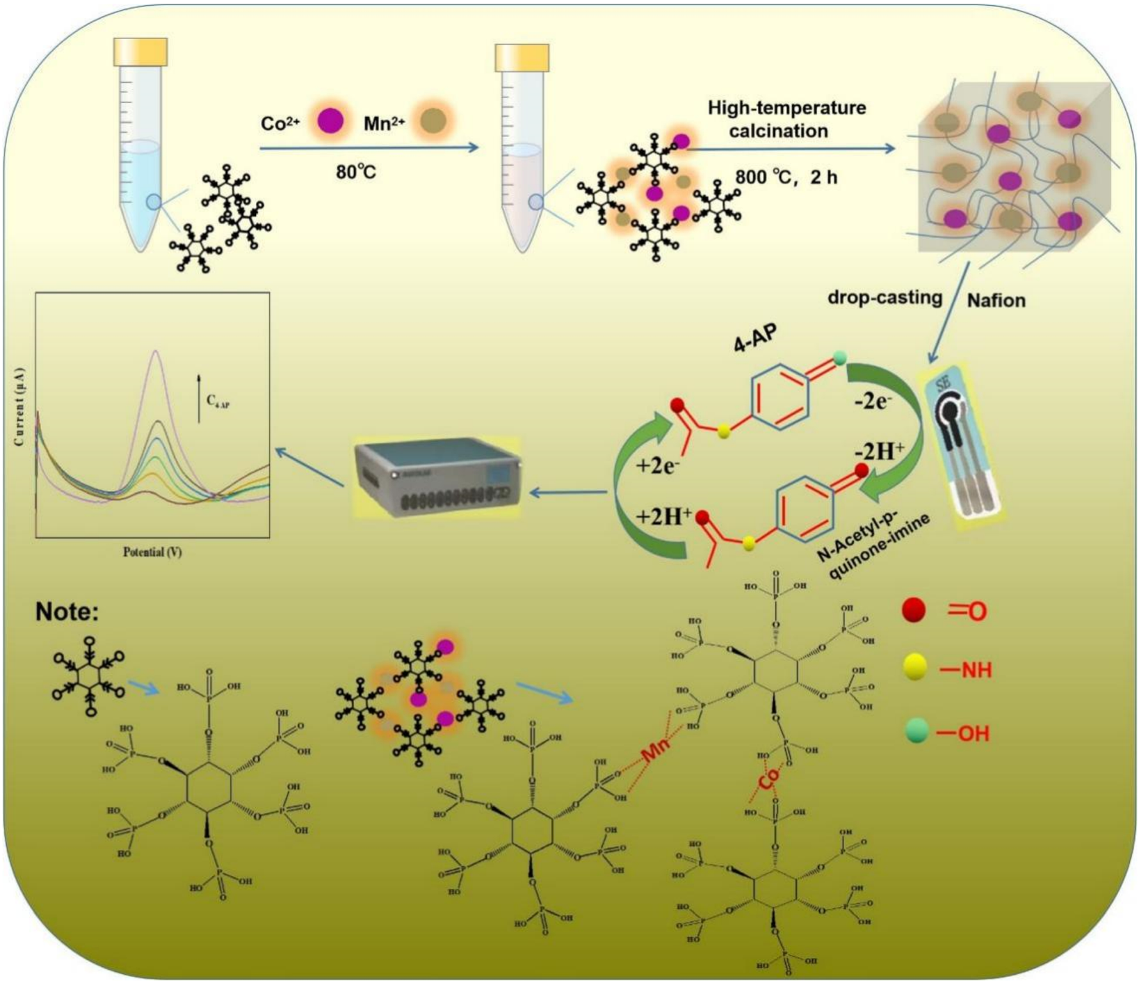

Scheme 1 Illustration of the synthesis of PA–CoMn-1 : x : 2 − x (x = 0, 0.5, 1 and 1.5) aerogel nanocomposite and the application of sensing 4-AP.

3 Results and discussion

3.1. XRD analysis

The crystallinity and structural property of PA–CoMn-1 : x : 2 − x (x = 0 and 1.5) aerogel were characterized by XRD. As displayed in Fig. 1, the diffraction peaks of PA–CoMn-1 : 1.5 : 0.5 aerogel matched well with the simulated PA–Co-1 : 2 and PA–Mn-1 : 2, whereby the diffraction peaks appearing at $2\theta = 29.60°$, $31.10°$ and $34.6°$ can be assigned to (011), (101) and (111), respectively.[30,31] The aerogel PA–Mn-1 : 2 exhibited a characteristic peak confirming the presence of Mn_2O_3 particles in the PA–CoMn-1 : 1.5 : 0.5 nanocomposite. Due to the presence of a small amount Mn_2O_3 in the PA–CoMn-1 : 1.5 : 0.5 nanocomposite, the XRD patterns of Mn_2O_3 NPs were relatively poor. The PXRD pattern of PA–FeCo-1 : 2 : 2 consisted of $Co_2P_4O_{12}$ (PDF#84-2208), revealing that PA–FeCo-1 : 2 : 2 had a $Co_2P_4O_{12}$ structure, which confirmed the successful fabrication of samples.

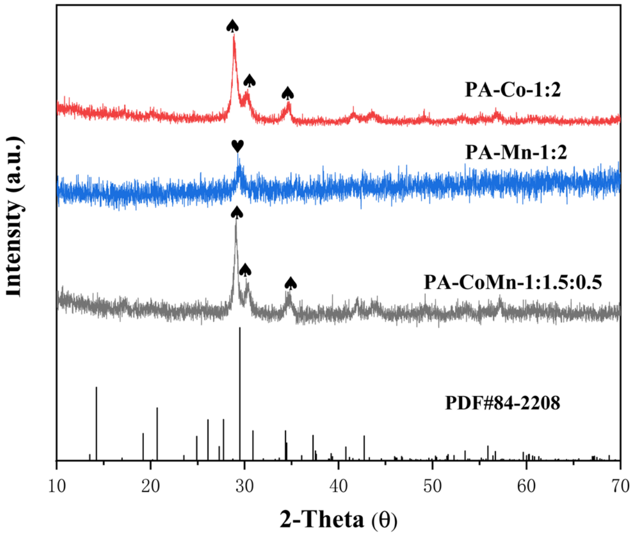

Fig. 1 PWXRD patterns of PA–Co-1 : 2, PA–Mn-1 : 2 and PA–CoMn-1 : 1.5 : 0.5 aerogel.

3.2. FESEM analysis

The morphology of the synthesized material and its composite were analyzed by SEM (Fig. 2). Single metal–PA aerogel of Mn and Co are shown in Fig. 2a and b. PA–Co-1 : 2 had

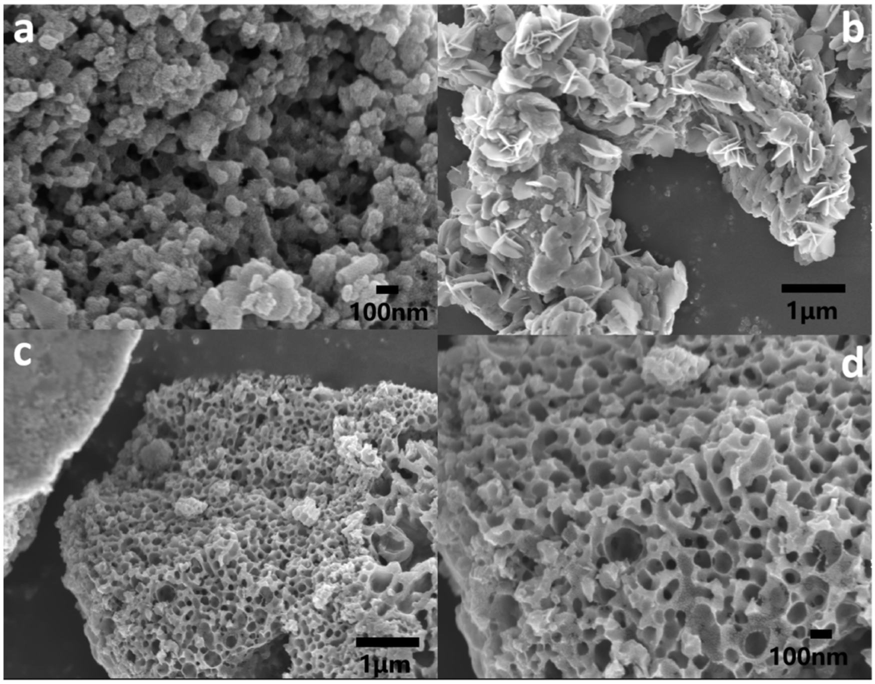

Fig. 2 SEM images of PA–Co-1 : 2 (a), PA–Mn-1 : 2 (b) and PA–CoMn-1 : 1.5 : 0.5 (c and d) aerogel.

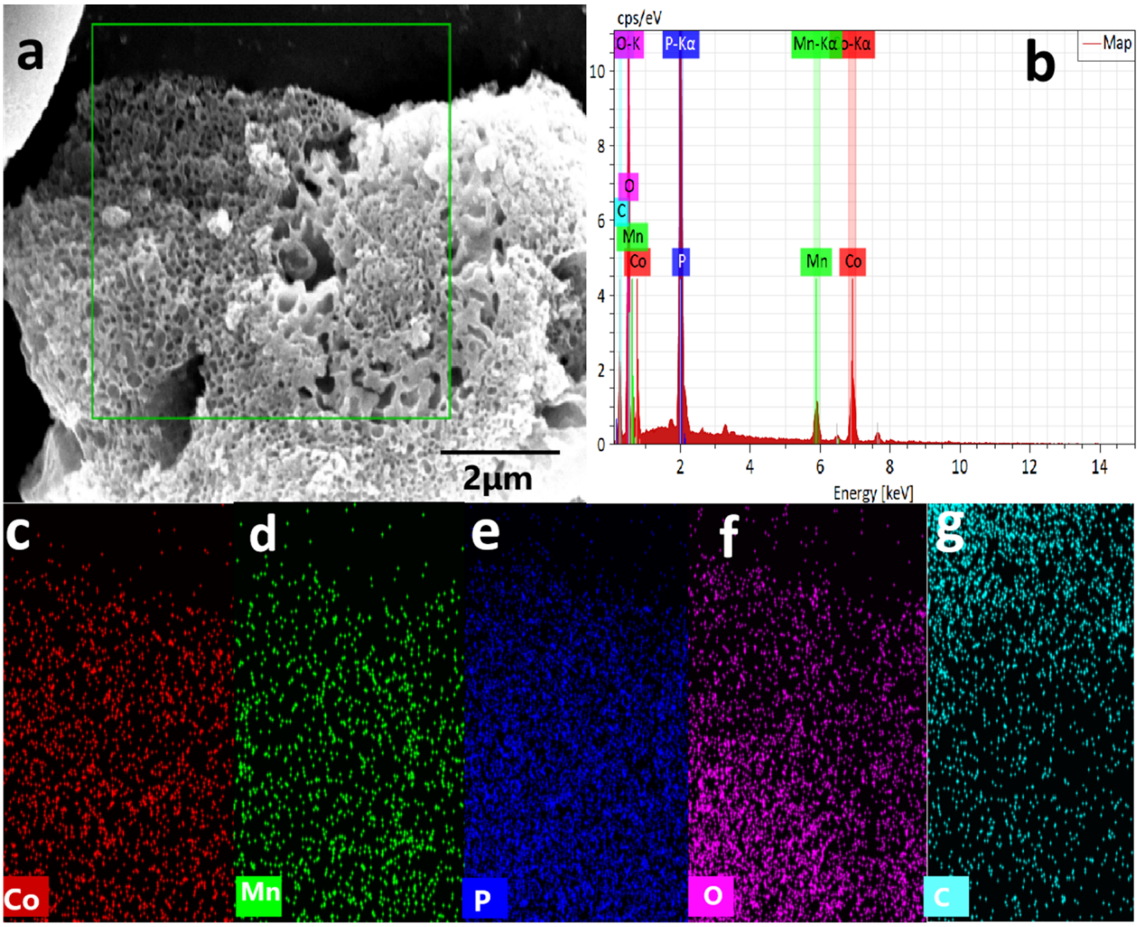

Fig. 3 EDS-based element district (a) and mapping images (Co, Mn, P, O and C) (c–g), (b) EDS spectrum of PA–FeCo-1 : 1.5 : 0.5 aerogel.

a morphology of cross-linked network structure aggregated by irregular nanoparticles, with a particle diameter of about 50 nm. PA–Co-1 : 2 exhibited a stacked three-dimensional structure composed of irregular nanosheets and nanoparticles. Compared with single metal–PA aerogel, the PA–CoMn-1 : 1.5 : 0.5 aerogel displayed a more tightly cross-linked porous structure, with irregular bore diameter (Fig. 2c and d). Moreover, the energy-dispersive spectroscopy (EDS) elemental mapping images and spectrum of PA–CoMn-1 : 1.5 : 0.5 demonstrated that Co, Mn, P, O and C elements were all present (Fig. 3a–g). This confirmed that PA–CoMn-1 : 1.5 : 0.5 was successfully prepared by high temperature carbonization. Moreover, TEM images of PA–CoMn-1 : 1.5 : 0.5 (Fig. 4a–c) aerogel and mapping images (Co, Mn, P, O and C) (g–i) are shown in Fig. S1(g–i).† The calculated lattice distance $d = 0.325$ nm is also correlated with the plane (111) in PA–CoMn-1 : 1.5 : 0.5 and matched with the XRD data.

3.3. FT-IR spectra

Fourier transform infrared spectroscopy (FT-IR) was used to further explore the detailed chemical structures of PA–CoMn-1 : x : $2-x$ ($x = 0$, 0.5, 1 and 1.5) aerogel (Fig. 5). Four bands appeared at 610 and 530 cm^{-1} which can be attributed to the asymmetric stretching and bending mode of vibrations of Mn–O.[32] The absorptions of PA–CoMn-1 : x : $2-x$ ($x = 0$, 0.5, 1 and 1.5) aerogel at 1510 and 1070 cm^{-1} are attributed to the stretching vibrations of P=O and P–O–C, respectively. It indicates that high temperature carbonization destroyed most of the P=O groups, which may be the cause of particle agglomeration.

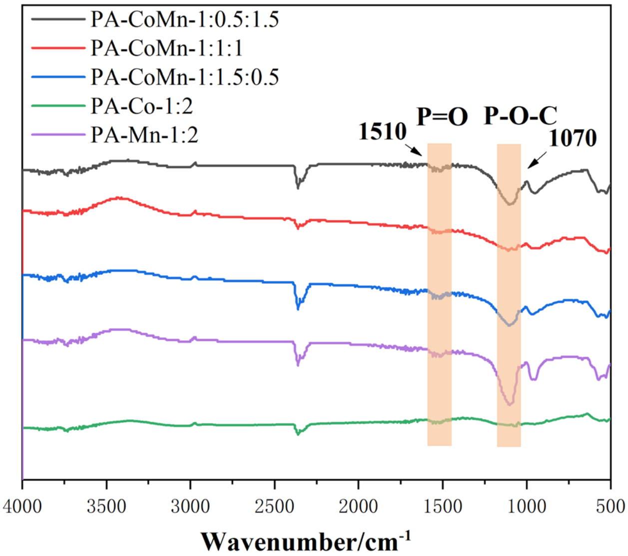

Fig. 5 FT-IR images of PA–CoMn-1 : x : $2-x$ ($x = 0$, 0.5, 1 and 1.5) aerogel.

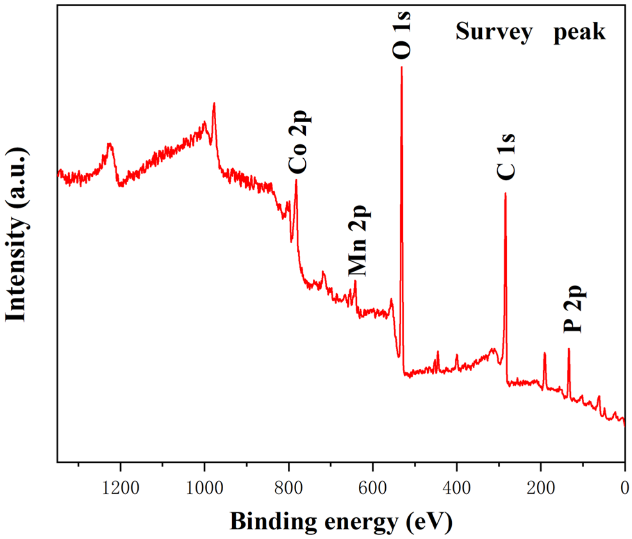

Fig. 6 XPS spectra of PA–CoMn-1 : 1.5 : 0.5 aerogel.

3.4. XPS spectra analysis

X-ray photoelectron spectroscopy (XPS) was utilized to explore elemental composition and surface chemical valence of PA–FeCo-1 : 1.5 : 0.5 aerogel. The obtained survey spectrum displayed in Fig. 6 confirmed the presence of Mn, Co, P, C & O elements. As shown in Fig. 7a, the C 1s high-resolution peak revealed that two types of carbon bond arise at binding energies of 284.48 and 286.42 eV for C–C and C–O bonds, respectively. The metal phosphide bond was confirmed with the high-resolution XPS peak of P 2p shown in Fig. 7b; a peak at 132.9 eV represents the existence of the Mn–P bond and Co–P, and another peak observed at 133.90 eV for the surface oxidation of metal phosphide. Fig. 7c displays the $2p_{1/2}$ orbital of Mn at the binding energies of 653.46 eV and 655.14 eV, followed by the $2p_{3/2}$ orbital of Mn at the binding energies of 641.71 eV and 643.83 eV, confirming the presence of Mn in both +2 and +3

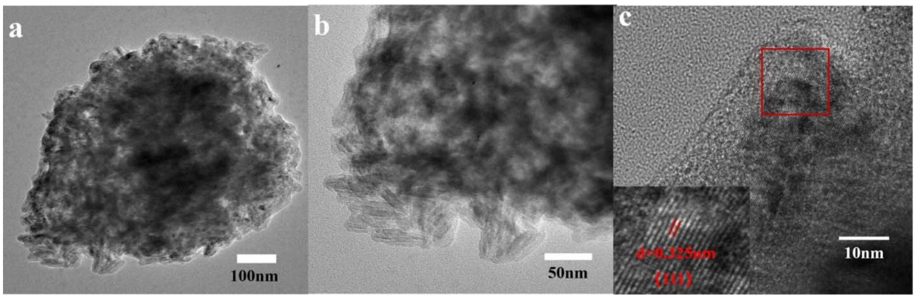

Fig. 4 (a–c) TEM images of PA–CoMn-1 : 1.5 : 0.5 aerogel.

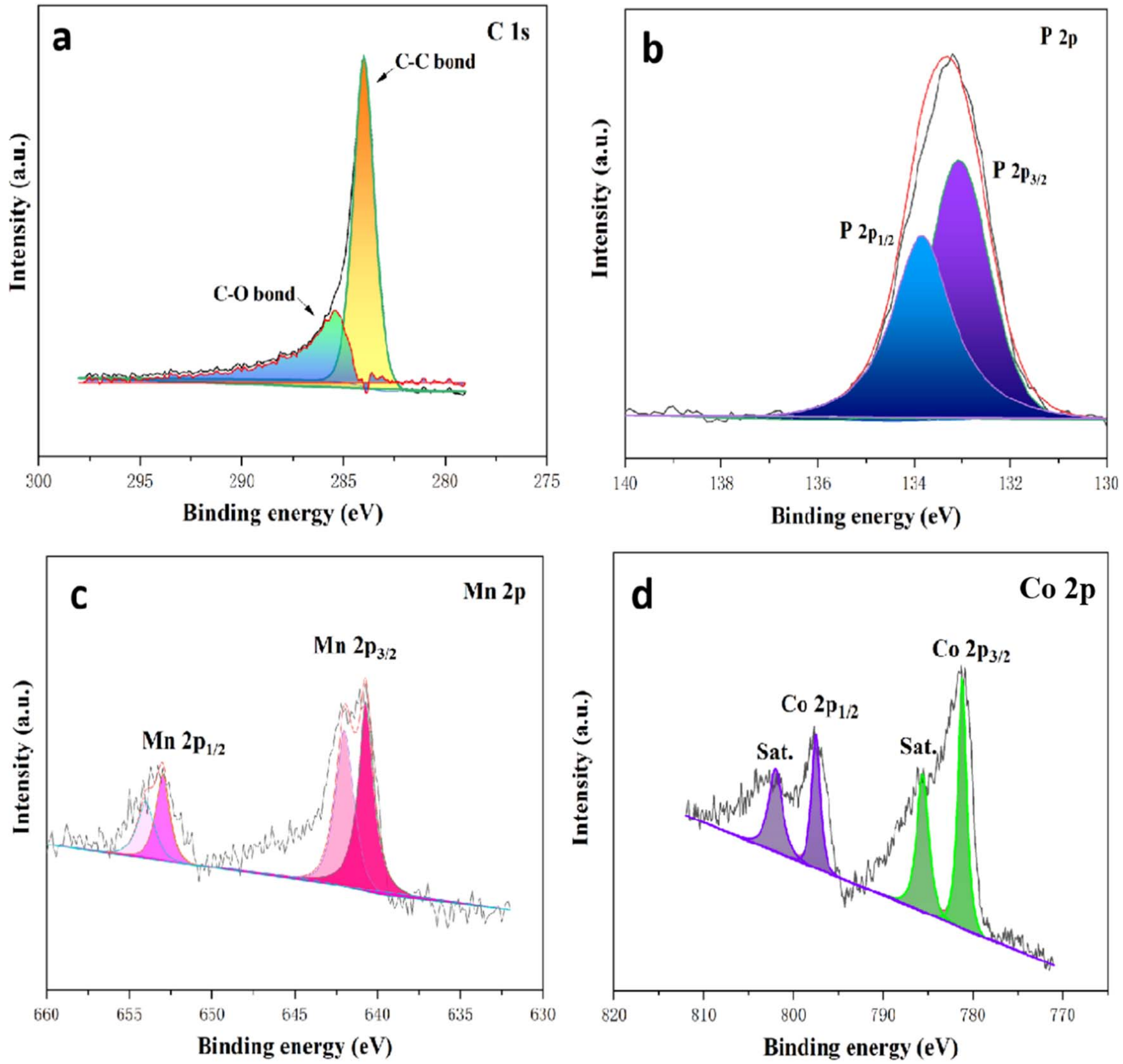

Fig. 7 Survey spectrum and high-resolution core spectrum for (a) C 1s, (b) P 2p, (c) Mn 2p and (d) Co 2p.

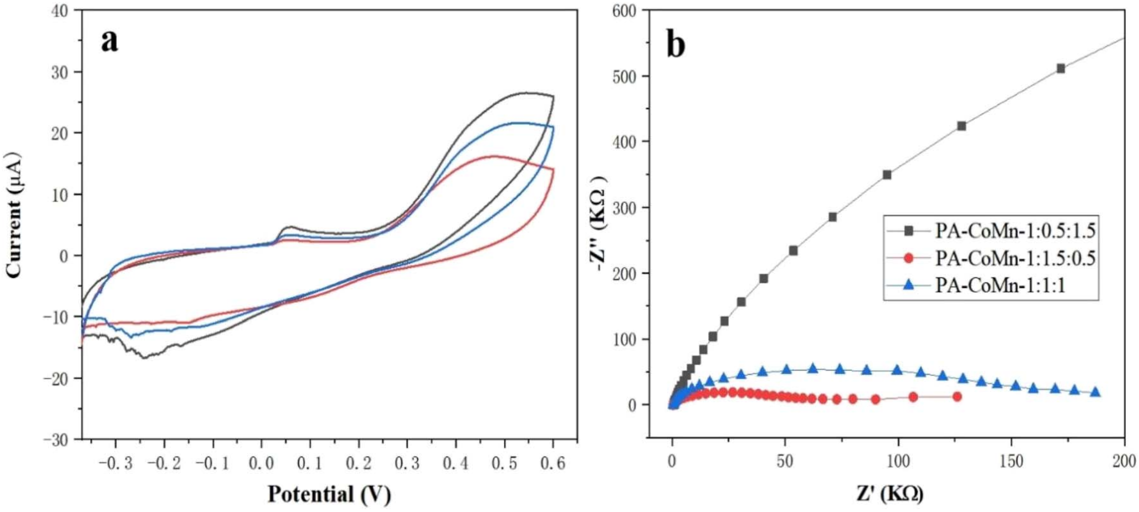

Fig. 8 (a) CV performance of PA–CoMn-1 : 0.5 : 1.5 (red), PA–CoMn-1 : 1 : 1.5 (blue) and PA–CoMn-1 : 1.5 : 0.5 (black) aerogel/SPCE and EIS (b).

oxidation states, respectively. The high-resolution XPS of Co 2p (Fig. 7d) exhibited main peaks at 781.01 eV and 796.64 eV attributed to Co $2p_{3/2}$ and Co $2p_{1/2}$ of Co in +2 state. Moreover, the two satellite peaks of Co-atom are observed at binding energies of 786.33 eV and 802.91 eV. As obtained in P 2p, the peaks confirm that PA effectively interacts with the MnCo through its affinity with the metal.

3.5. Electrochemical characterization

3.5.1. Electrocatalysis of modified electrodes. The electrocatalytic performance of the PA–CoMn-1 : x : 2 − x (x = 0.5, 1 and 1.5) aerogel/SPCE sensors was analyzed using cyclic voltammetry(CV). The sensor orderly was investigated in the presence of 0.1 M KCl and 5 mM $[\mathrm{Fe\ (CN)_6}]^{3-/4-}$ redox probe electrolyte. The CV electrocatalytic performances of PA–CoMn-1 : x : 2 − x (x = 0.5, 1 and 1.5) aerogel/SPCE sensor can be seen in Fig. 8a, which shows the electron charge conductivity of varied modified electrodes. From Fig. 8a, the PA–CoMn-1 : 1.5 : 0.5 aerogel/SPCE(black) exhibited electrocatalytic activity in the presence of a 5 mM $[\mathrm{Fe(CN)_6}]^{3-/4-}$ redox probe. Therefore, the modified electrodes resulted in high electron charge and rapid electron transfer between the electrode and the electrolyte. Furthermore, the electron transport capacity of modified electrodes was further evaluated by EIS as shown in Fig. 8b. The Nyquist plot was obtained with an open circuit potential of 0.20 V. The charge transfer resistance (R_{ct}) calculated from the diameter of the semicircle, notably the smaller semicircle exhibited by the PA–CoMn-1 : 1.5 : 0.5 aerogel/SPCE shows a higher rate of electron transfer in electrochemical performance. This may be ascribed to the fact that Co–P bonds were generated and increased the electron carrier mobility.

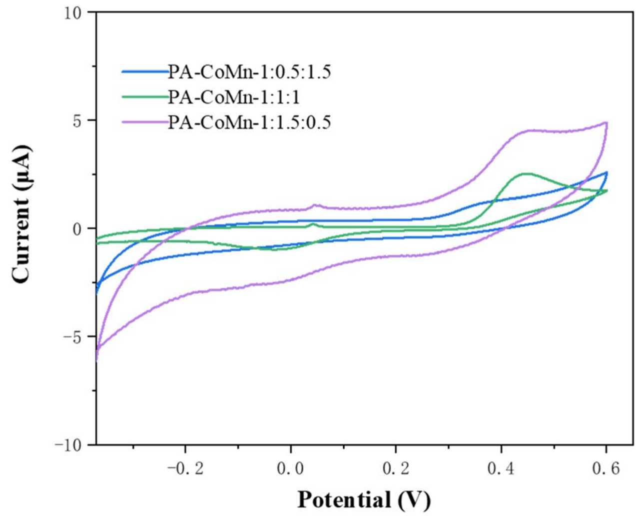

Fig. 9 CV performance of PA–CoMn-1 : x : 2 − x (x = 0.5, 1 and 1.5) aerogel/SPCE in 100 μM 4-AP.

Electrochemical investigation of modified electrodes was performed to test for catalytic performance using CV towards the 4-AP, it is performed with the 100 μM of 4-AP on 0.1 M PBS solution. As displayed in Fig. 9, PA–CoMn-1 : 1.5 : 0.5 aerogel/SPCE has the highest catalytic activity in the electrochemical redox performance of 4-AP than the PA–CoMn-1 : 1 : 1 and PA–CoMn-1 : 0.5 : 1.5 aerogels.

3.5.2. Effect of scan rate. To investigate the reaction kinetics of the modified electrode, the influence of scan rate was performed. Fig. 10a portrayed the CV curve of 100 μM 4-AP in 0.1 M of PBS at different scan rates varies from 10 to 200 mV s^{-1}. It can be seen that the reduction peak intensity linearly increases with increase in scan rates. Furthermore, the relationship between oxidation peak current and scan rate were plotted and the correlation coefficient values from the linear relationship for anodic current and the cathodic current were obtained as I (μA) = 0.0446x + 1.5909, R^2 = 0.9908 and I (μA) = −0.0249x + 1.229R^2 = 0.9949 respectively (Fig. 10b) which illustrates that the oxidation of 4-AP on PA–CoMn-1 : 1.5 : 0.5 aerogel/SPCE was a surface controlled process.

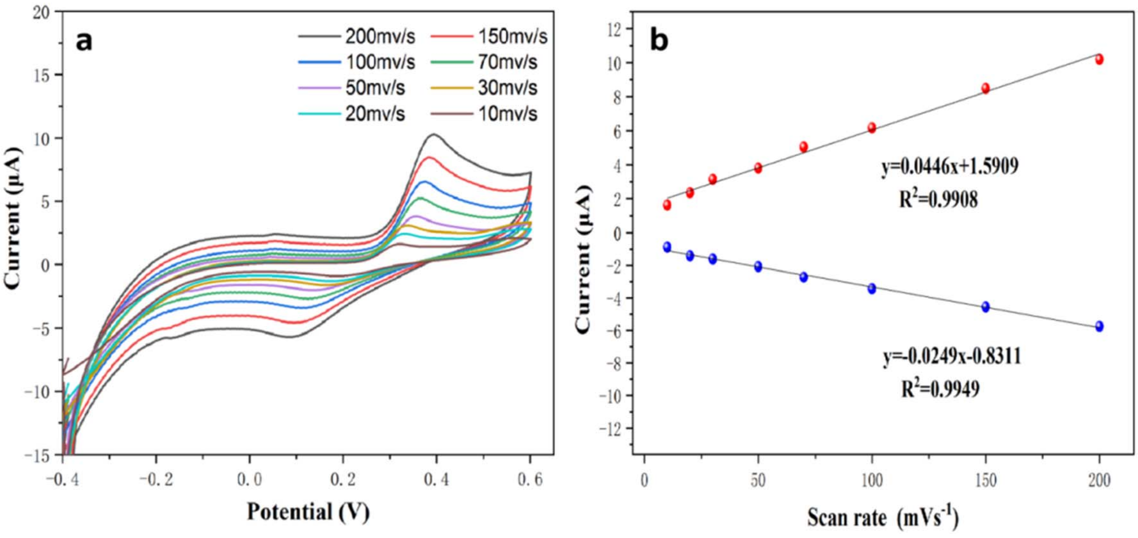

Fig. 10 (a) The different scan rate CV performances using PA–CoMn-1 : 1.5 : 0.5 aerogel/SPCE from the range of 10 to 200 mV s^{-1} and (b) their scan rate against its current response linear plot.

3.5.3. Influence of different pH. To elucidate the 4-AP oxidation mechanism, the pH effect was investigated for pH range 6.5–9.0 using 50 μM 4-AP with CV test. In Fig. 11, the current peak of 4-AP was shown in the bar chart, which showed varied pH of PBS buffer solution have no significant impact on sensing 4-AP. Furthermore, the pH = 7.5 value was utilized for further experiments.

3.5.4. Quantitative analysis. DPV was employed for the sensitive detection of PA–CoMn-1 : 1.5 : 0.5 aerogel/SPCE and was recorded by varying the concentrations of 4-AP in 0.1 M PBS (pH 7.5) at a scan rate of 100 mV s^{-1}. Fig. 12a shows the response of DPV curve for the oxidation of 4-AP with different initial concentrations with optimal condition. Here at lower concentration, a sharp oxidation peak potential was obtained at 0.39 V. It can be witnessed that the oxidation peak current linearly increases with increase in the 4-AP concentration from 1 μM to 0.1 mM. Besides, a linear plot of reduction current *versus* the concentration of 4-AP displayed two linear relationships in the range of 1 μM to 0.1 mM (Fig. 12b). The corresponding linear equation with correlation coefficient was expressed as $I\,(\mu A) = 0.098 + 0.07C_{4\text{-AP}}$, $R^2 = 0.9956$. Further, the lowest limit of detection (LOD) was calculated from the lowest concentration using the following eqn (1).

$$\text{LOD} = 3\sigma/\text{slope} \tag{1}$$

where σ specifies the standard deviation response from the lowest concentration and slope denotes the slope obtained from the calibration curve. The slope value from the first linear equation is 0.07 and the LOD was found to be 0.2133 μM. A comparison of our sensor with the previously reported sensor is presented in Table 1.

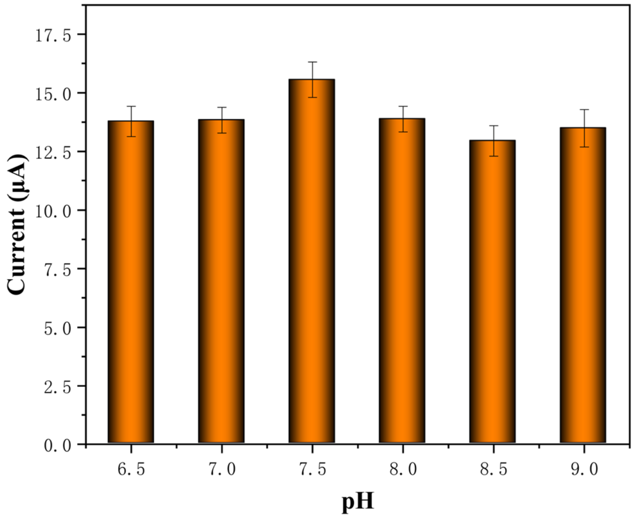

Fig. 11 Graphical plot of PA–CoMn-1 : 1.5 : 0.5 aerogel/SPCE in 0.1 M of different pH (6.5–9) solutions containing 50 μM of 4-AP at scan rate 50 mV s^{-1}.

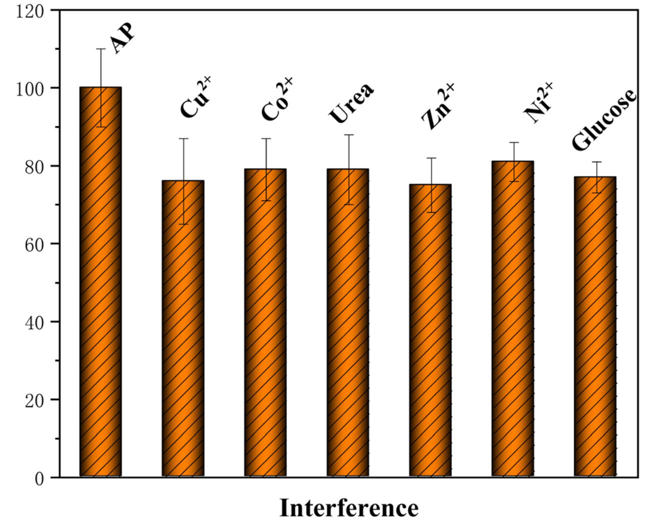

Fig. 13 Selectivity of PA–CoMn-1 : 1.5 : 0.5 aerogel/SPCE toward 4-AP (50 μM) in the presence of 10-fold concentration of different interfering substances.

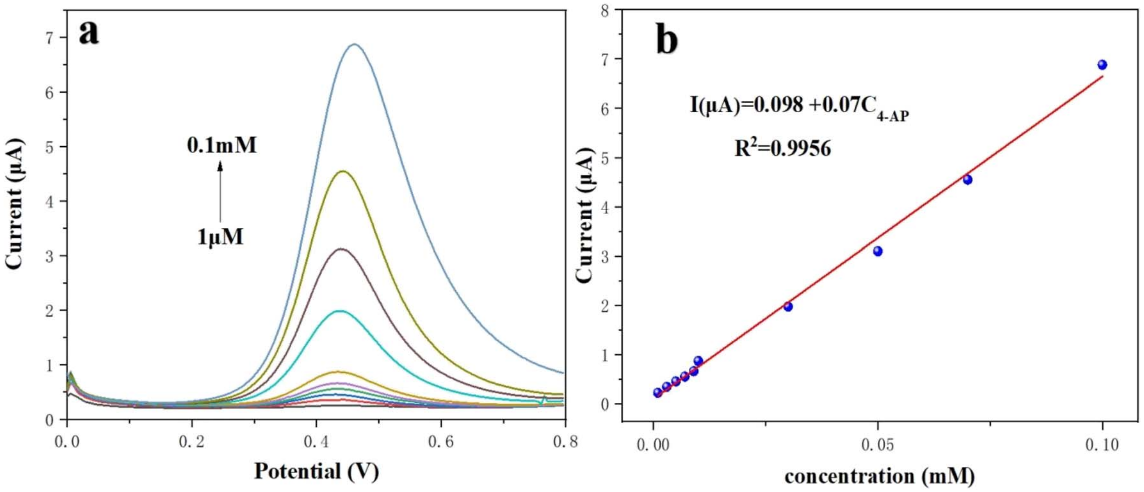

Fig. 12 (a) DPV responses of PA–CoMn-1 : 1.5 : 0.5 aerogel/SPCE in 0.1 M pH 7.5 solution by successive addition of 4-AP (1 μM to 0.1 mM). (b) Linear plot of current response *vs.* 4-AP.

Table 1 Comparison of 4-AP determination with different electrodes[a]

Sensors	Methods	Linear range	LOD	References
Hollow Fe_3O_4–rGO/GCE	SWV	5×10^{-7} to 10^{-4} M	0.11 μM	33
Ag-ZIF-67/GCE	DPV	0.1–70.0 μM	0.04 μM	34
Sa-TN50/$Cu_3(BTC)_2$/GCE	DPV	4.0–153.0 μM	0.7 μM	35
Lt/fMWCNT	DPV	0.9–80 μM	0.78 μM	36
NiO–CuO/GR	SWV	4.0–400 μM	1.33 μM	37
MB/Cu/N–C/GCE	SWV	0.5–150.0 μM	0.4 μM	38
AuNP–PGA/SWCNT film	DPV	50–300 μM	15.0 μM	39
FeNi/rGO/GCE	DPV	1–100 μM, 100–3000 μM	0.3 μM	40
PA–CoMn-1 : x : 2 − x (x = 0, 0.5, 1 and 1.5)/SPCE	DPV	1 μM to 0.1 mM	0.2133 μM	This work

[a] 1,3,5-Triformylphloroglucinol (TFP) and 2,6-diaminoanthraquinone (DAAQ) and named as TFP–DAAQ-COF, Lt/fMWCNT = luteolin on a functionalized multi-wall carbon nanotube.

Table 2 Real sample analysis for the determination of 4-AP in drug samples (n = 3)

	4-AP concentration			
Sample	Added (μM)	Found (μM)	Recovery (%)	RSD (%)
Commercial drug	0	0	0	0
	5	6.83	97.57	1.43 ± 0.12
	10	11.87	98.91	1.81 ± 0.17
	20	21.85	99.32	2.15 ± 0.21

3.5.5. Selectivity, stability and reproducibility of PA–CoMn-1 : 1.5 : 0.5 aerogel/SPCE modified SPCE. To investigate the anti-interference capability of PA–CoMn-1 : 1.5 : 0.5 aerogel/SPCE, the corresponding graphical bar diagram is shown in Fig. 13. The graph shows the effect of 10-fold concentrations of $ZnCl_2$, $CuCl_2$, $Co(NO_3)_2 \cdot 6H_2O$, $NiCl_2 \cdot 6H_2O$, urea and glucose on the electrochemical response of 50 μM 4-AP. There is no considerable change in the electrochemical peak current of 4-AP and the influence of interference species on 4-AP detection is less than 5%. Therefore, the proposed PA–CoMn-1 : 1.5 : 0.5 aerogel/SPCE shows good selectivity towards 4-AP sensor in (pH 7.5) PBS. The storage stability of the proposed sensor was determined using the same electrode for different number of days, which also showed peculiar results with limited change in the current.

3.5.6. Actual sample analysis. The 4-AP tablets (250 mg per tablet, 4-AP 70% wt) used in the experiment were purchased from a pharmacy. First, each tablet was well ground and dissolved in water by stirring. Next, the tablet solution was diluted with 1000 mL 0.1 M PBS (pH 7.5) giving a 2 μM concentration of 4-AP for electrochemical detection. The actual sample analysis of PA–CoMn-1 : 1.5 : 0.5 aerogel/SPCE was investigated using DPV performance with the addition of 0, 5, 10, and 20 μM of 4-AP to 0.1 M PBS solution. In general, the standard addition method was used to detect the 4-AP in the real drug sample. The data obtained are collectively exhibited in Table 2.

4 Conclusion

In summary, the PA–CoMn-1 : x : 2 − x (x = 0, 0.5, 1 and 1.5) aerogel was successfully prepared and applied in 4-AP sensing in real drug samples with excellent accuracy and applicability, demonstrating its practical precision and superb serviceability. Furthermore, the PA–CoMn-1 : x : 2 − x (x = 0, 0.5, 1 and 1.5) aerogel/SPCE exhibited satisfactory selectivity and stability, providing a great potential platform for the construction of 4-AP sensor in varied practical samples and complicated environments.

Data availability

Data for the study is openly available in a public repository.

Author contributions

H. J. Guo planned the experiments, conducted the experiments, and wrote the paper draft. Y. F. Qi supported and discussed the manuscript. G. X. Wang and Y. Zhang draw pictures of manuscript. S. Q. Li and B. Y. Tan analyzed the data.

Conflicts of interest

The authors declare no conflict of interest.

Acknowledgements

The authors gratefully acknowledge financial support from Jilin Provincial Department of Science and Technology Project [2021020142GX].

References

1 E. A. Suarez, M. Nguyen, D. Zhang, *et al.*, Novel methods for pregnancy drug safety surveillance in the FDA Sentinel System, *Pharmacoepidemiol. Drug Saf.*, 2023, **32**(2), 126–136.
2 D. G. Serota, Book Review: Drug Safety Evaluation, Fourth Edition, *Int. J. Toxicol.*, 2023, (4), 366–367.
3 A. Clary, N. D. Lin, T. Lasky, *et al.*, Considerations for defining medication exposure when analyzing real-world data, *Pharmacoepidemiol. Drug Saf.*, 2023, **32**(8), 933–937.
4 I. Manov, H. Motanis, I. Frumin, *et al.*, Hepatotoxicity of anti-inflammatory and analgesic drugs: ultrastructural aspects, *Acta Pharmacol. Sin.*, 2010, **27**(003), 259–272.

5 J. R. Medina, A. Licea and M. Hurtado, An improved micromethod for plasma determination of acetaminophen by visible spectrophotometry: application to a pharmacokinetic study in rabbits, *Int. J. Pharm.*, 2017, **9**(4), 96–98.

6 S. F. Cook, A. D. King, Y. Chang, *et al.*, Quantification of a biomarker of acetaminophen protein adducts in human serum by high-performance liquid chromatography-electrospray ionization-tandem mass spectrometry: clinical and animal model applications, *J. Chromatogr. B: Anal. Technol. Biomed. Life Sci.*, 2015, **985**, 131–141.

7 Y. J. Chao, L. X. Xie and W. Cao, Chemiluminescence enhancement effect for the determination of acetaminophen with the catalysis of manganese deuteroporphyrin, *Key Eng. Mater.*, 2014, **575–576**, 249–252.

8 H. Montaseri and P. B. C. Forbes, Fluorescence sensor probe for the detection of acetaminophen using L-cysteine CdSe/ZnS quantum dots and molecular imprinted polymer@quantum dots, *IEEE Sens.*, 2017, 1–3.

9 Y. C. Liu, S. W. Chang, C. Y. Chen, *et al.*, Separation and determination of cold medicine ingredients by capillary zone electrophoresis using sulfated β-cyclodextrin as an electrolyte modifier and chiral selector, *J. Chin. Chem. Soc.*, 2015, **62**(2), 191–196.

10 R. Zhang, G. van Straaten, V. Di Palma, *et al.*, Electrochemical activation of atomic layer-deposited cobalt phosphate electrocatalysts for water oxidation, *ACS Catal.*, 2021, **11**(5), 2774–2785.

11 S. Jiang, L. Zhu, Z. Yang, *et al.*, Enhanced electrocatalytic performance of FeNiCoP amorphous alloys as oxygen-evolving catalysts for electrolytic water splitting application, *Electrochim. Acta*, 2021, **368**, 137618.

12 X. Ding, A. Li, F. Yang, *et al.*, Beta-tricalcium phosphate and octacalcium phosphate composite bioceramic material for bone tissue engineering, *J. Biomater. Appl.*, 2020, **9**, 34.

13 L. Zhang, J. Peng, W. Zhang, *et al.*, Rational introduction of borate and phosphate ions on $NiCo_2O_4$ surface for high-efficiency overall water splitting, *J. Power Sources*, 2021, **490**, 229541.

14 S. Kagaya, M. Saiki, A. M. Zanariah, *et al.*, Separation of Lead from Iron Matrix by Coprecipitation with Lanthanum Phosphate for ICP-AES Determination, *J. Ecotech. Res.*, 2005, **11**(4), 165–168.

15 S. S. Nandi, V. Adimule, S. A. Kadapure, *et al.*, Rare Earth Based Nanocomposite Materials for Prominent Performance Supercapacitor: A Review, *Appl. Mech. Mater.*, 2022, **908**, 3–18.

16 S. Liang, H. Wang, Y. Li, *et al.*, Rare-earth based nanomaterials and their composites as electrode materials for high performance supercapacitors: a review, *Sustainable Energy Fuels*, 2020, **4**(8), 3825–3847.

17 C. Gao, X. Guo, L. Nie, *et al.*, A simple and rapid electrodeposition method to prepare seed layer of WOX on the ITO glass for solvothermal synthesis of WO_3 nanowires film, *Mater. Lett.*, 2022, **328**, 133136.

18 S. D. Han, J. X. Hu, J. H. Li, *et al.*, Anchoring polydentate N/O-ligands in metal phosphite/phosphate/phosphonate (MPO) for functional hybrid materials, *Coord. Chem. Rev.*, 2023, **475**, 214892.

19 P. A. Shabadrov, A. P. Safronov, N. M. Kurilova, *et al.*, Design of Spherical Gel-Based Magnetic Composites: Synthesis and Characterization, *J. Compos. Sci.*, 2023, **7**(5), 177.

20 S. R. Murugavel, Compositional control as the key for achieving highly efficient OER electrocatalysis with cobalt phosphates decorated nanocarbon florets, *Small*, 2020, **16**(12), 1903334.

21 M. M. Khalaf, H. M. El-Lateef, A. Touny, *et al.*, Electrocatalytic performance of inorganic nanoflakes nickel phosphates under adjusted synthetic parameters towards urea and methanol oxidation in alkaline media, *Microchem. J.*, 2021, **163**, 105901.

22 P. Bhanja, Y. Kim, B. Paul, *et al.*, Facile synthesis of nanoporous transition metal-based phosphates for oxygen evolution reaction, *ChemCatChem*, 2020, **12**(7), 2091–2096.

23 D. S. García, J. Q. Bermejo and J. C. Gutierrez, Green and easy synthesis of P-doped carbon-based hydrogen evolution reaction electrocatalysts, *Carbon*, 2023, **212**, 118154.

24 Y. Huo, M. Bu, Z. Ma, *et al.*, Flexible, non-contact and multifunctional humidity sensors based on two-dimensional phytic acid doped co-metal organic frameworks nanosheets, *J. Colloid Interface Sci.*, 2022, **607**, 2010–2018.

25 X. Feng, Y. L. Xiao, H. H. Huang, *et al.*, Phytic Acid-Based FeCo Bimetallic Metal-Organic Gels for Electrocatalytic Oxygen Evolution Reaction, *Chem.–Asian J.*, 2021, **16**(20), 3213–3220.

26 T. Zhang, T. Yang, B. Li, *et al.*, MOF-derived formation of ultrafine FeP nanoparticles confined by N/P Co-doped carbon as an efficient and stable electrocatalyst for hydrogen evolution reaction, *Appl. Surf. Sci.*, 2022, **597**, 153662.

27 L. Ye, Y. Ying, D. Sun, *et al.*, Ultrafine Mo_2C nanoparticles embedded in an MOF derived N and P co-doped carbon matrix for an efficient electrocatalytic oxygen reduction reaction in zinc–air batteries, *Nanoscale*, 2022, **14**(5), 2065–2073.

28 Y. J. Wang, L. Lu, R. X. Tu, *et al.*, Introduction of Cascade Biocatalysis Systems into Metal–Organic Aerogel Nanostructures for Colorimetric Sensing of Glucose, *ACS Appl. Nano Mater.*, 2022, **5**(6), 8154–8160.

29 X. Niu, J. Y. Lin, X. J. Bo, *et al.*, Preparation of a novel Ni-MOF and porous graphene aerogel composite and application for simultaneous electrochemical determination of nitrochlorobenzene isomers with partial least squares, *Microchim. Acta*, 2020, **187**(7), 1–10.

30 J. Wu, Q. Wang, A. Umar, *et al.*, Highly sensitive P-nitrophenol chemical sensor based on crystalline α-MnO_2 nanotubes, *New J. Chem.*, 2014, **38**(9), 4420–4426.

31 M. M. Rahman, M. M. Alam and A. M. Asiri, Detection of toxic choline based on Mn_2O_3/NiO nanomaterials by an electrochemical method, *RSC Adv.*, 2019, **9**(60), 35146–35157.

32 J. Ahmed, M. Faisal, S. A. Alsareii, *et al.*, Mn_2O_3 nanoparticle-porous silicon nanocomposite based amperometric sensor

for sensitive detection and quantification of Acetaminophen in real samples, *Ceram. Int.*, 2023, **49**(1), 933–943.

33 L. Shen, J. Dong, B. Wen, *et al.*, Facile Synthesis of Hollow Fe_3O_4-rGO Nanocomposites for the Electrochemical Detection of Acetaminophen, *Nanomaterials*, 2023, **13**(4), 707.

34 J. Wang, F. Yin, W. Tang, *et al.*, Electrochemical detection of acetaminophen and caffeine using Ag nanoparticles doped metal-organic framework (ZIF-67) composites, *Int. J. Electrochem. Sci.*, 2023, **18**(11), 100334.

35 E. Mouafo-Tchinda, J. C. Kemmegne-Mbouguen, C. P. Nanseu-Njiki, *et al.*, Solvothermal synthesis of organoclay/Cu-MOF composite and its application in film modified GCE for simultaneous electrochemical detection of deoxyepinephrine, acetaminophen and tyrosine, *RSC Adv.*, 2023, **13**(30), 20816–20829.

36 M. Amiri-Aref, J. B. Raoof and R. Ojani, A highly sensitive electrochemical sensor for simultaneous voltammetric determination of noradrenaline, acetaminophen, xanthine and caffeine based on a flavonoid nanostructured modified glassy carbon electrode, *Sens. Actuators, B*, 2014, **192**, 634–641.

37 B. Liu, X. Ouyang, Y. Ding, *et al.*, Electrochemical preparation of nickel and copper oxides-decorated graphene composite for simultaneous determination of dopamine, acetaminophen and tryptophan, *Talanta*, 2016, **146**, 114–121.

38 Y. Li, X. Liu and J. Zheng, A dual-ratiometric electrochemical sensor based on Cu/N-doped porous carbon derived from Cu-metal organic framework for acetaminophen determination, *Microchem. J.*, 2023, **189**, 108556.

39 S. H. Lee, J. H. Lee, V.-K. Tran, *et al.*, Determination of acetaminophen using functional paper-based electrochemical devices, *Sens. Actuators, B*, 2016, **232**, 514–522.

40 Y. Yan, S. Zeng, F. Xu, *et al.*, Electrochemical Determination of Acetaminophen with a FeNi Nanoparticle Reduced Graphene Oxide (rGO) Nanocomposite and Differential Pulse Voltammetry (DPV), *Anal. Lett.*, 2024, **57**, 996–1007.